Delft University of Technology

Rational hyperelastic modelling of elastic poured compound for the failure analysis of embedded rail system

Wang, Li; Li, Shaoguang; Wang, Ping; Chen, Rong; Li, Zili

Important note
To cite this publication, please use the final published version (if applicable).
Please check the document version above.

Taylor & Francis
Taylor & Francis Group

🔓 OPEN ACCESS | Check for updates

Rational hyperelastic modelling of elastic poured compound for the failure analysis of embedded rail system

Li Wang [ID][a,b], Shaoguang Li[b], Ping Wang [ID][a], Rong Chen[a] and Zili Li[b]

[a]Ministry of Education, Key Laboratory of High-Speed Railway Engineering, Southwest Jiaotong University, Chengdu, China; [b]Section of Railway Engineering, Department of Engineering Structures, Faculty of Civil Engineering and Geosciences, Delft University of Technology, Delft, The Netherlands

ABSTRACT

The continuous homogeneous rail constraint of embedded rail system (ERS) is realized by the encapsulation of rails with the elastic poured compound (EPC) which is a composite material. Previous treatment of EPC as linear elastic material was insufficient in the failure analysis of ERS. In this work, a hyperelastic model is developed to describe the mechanical properties of the EPC with engineering strain up to 150%. Physical tests of uniaxial tension, planar tension and quadruple shear are conducted. A 4-parameter Ogden model is determined by curve fitting and validated with a progressive validation strategy, and then is applied to the failure analysis of ERS. It is found that the material nonlinearity of EPC contributes noticeably to the decrease of the longitudinal stiffness of ERS. The 2nd debonding is more probably caused by the failure of adhesive at the interface between EPC and rail rather than EPC itself.

1. Introduction

Embedded rail system (ERS) is a type of non-ballast track structure that has so far mainly been used in tram lines in urban areas [1,2]. To reduce noise and vibration, the rail is usually enclosed with elastomers, including a rubber strip right under the rail and an elastic poured compound (EPC, also called Corkelast [1]) which surrounds almost the whole rail except the rail head, as shown in Figure 1. The rail and the elastomers are embedded together in a concrete or steel groove to provide an obstacle-free surface for sharing road rights with road traffic and pedestrians. One more distinguishing characteristic of ERS is its special rail support mechanism. Rather than the discrete support by fasteners that the traditional railway tracks usually have, ERS is able to realize continuous rail support by embracing along the rail with the homogeneous elastomers. ERS thus has no additional dynamic force due to bending between discrete rail supports [1]. With this concept, the application of ERS is extending to metros and high-speed railways [1]. Figure 1 shows its application in a metro.

In addition to providing continuous homogeneous rail support, EPC plays a key role in constraining rail deflection, inclination and longitudinal movement under train loading. With various thickness and hardness, the rubber strip primarily serves to adjust the vertical track stiffness. EPC is a multicomponent particle-reinforced composite, composed of rubber particles, polyurethanes, cork and some other additives [1,3]. By thoroughly mixing the components with a certain
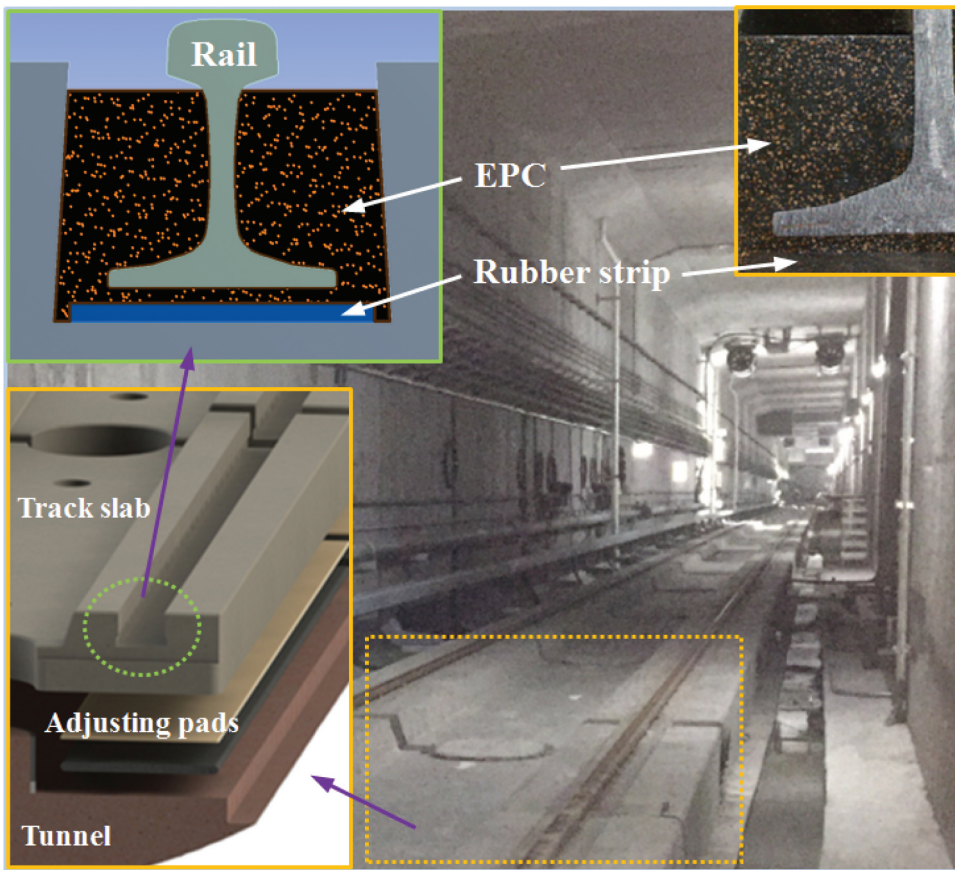
Figure 1. Typical embedded rail system in a newly built metro in China.

ratio, the EPC is prepared in the liquid state, and solidifies gradually within several hours [3]. During construction, after geometry adjustment and stress free of the rail in the concrete groove in the track slab, the EPC is poured into the groove and fills in all the void space. After solidification, the spatial constraint on the rail is formed. Usually, the main composition of EPC is determined by the need for track stiffness. In railway engineering, stiffness is one of the basic performance parameters in track structure design [4–6]. Wang et al. [5] studied the reasonable track stiffness and its design method for embedded rail structure used in metros. The elastic modulus of EPC was roughly determined to be about 5–9 MPa on the condition that EPC could be considered as linear elastic material.

In the literature, the EPC (or Corkelast) was usually considered as linear elastic or viscoelastic material [7–15]. De Man et al. [10] investigated the dynamic behaviour of various ERS by hammer tests and simulations. Zhao et al. [11]. developed a finite element model to predict the vibration and noise response of an ERS. Han et al. [12] studied the effect of control measures on wheel/rail noise, where the EPC was simulated in a mass-spring-damping subsystem, and represented by a mass and several linear spring and damper pairs. Yang et al. [13] investigated the wheel-rail impact-induced dynamic behaviour at an insulated rail joint used in ERS, and the linear viscoelasticity of EPC was considered. Stančík et al. [14] investigated the effects of temperature and loading rate on the ERS, where the nonlinearity of Corkelast was considered. However, these considerations are not enough when large deformation happens. In the authors' previous work [15], the failure behaviour of EPC

was investigated and it showed that the linear elastic treatment of EPC failed to simulate the failure behaviour because the EPC underwent large deformation.

Both quasi-static and dynamic rail movements can induce large shear deformation of EPC. Because of the constraint of rail movements by the groove, the deformations of EPC are limited in both the vertical and transverse directions. However, in the longitudinal direction, there is no sufficient limitation to rail movements. Thus, EPC is possible to undergo large deformation under longitudinal loads such as rail elongation or contraction due to temperature changes. Moreover, the tests in [5] show that the EPC is able to return from large deformation to its initial configuration without considerable permanent deformation when the load is removed. Thus, this behaviour of EPC is typical hyperelasticity, similar to that of rubber or rubber-like materials, as described in [16–18].

In recent decades, dozens of hyperelastic models have been developed [19–24], such as the Mooney-Rivlin [25–28], Ogden [29], Yeoh [30] and Arruda-Boyce models [31]. However, EPC is quite different from traditional rubber or rubber-like materials because EPC is a composite that contains various materials with different properties. Determining a constitutive model of one material is not sufficient to describe the behaviour of the whole composite [32,33]. Furthermore, the mechanical properties of EPC, such as stretch strength and shear strength, show uncertainties in lab tests most probably because of the multi-composition and tiny bubbles introduced in the chemical reaction combining the prepolymer and the catalyst [3]. The situation could be even more serious in practical complex constructions. All these factors make the hyperelastic modelling of EPC different from that of traditional hyperelastic materials.

Based on finite strain theory (see Section 2), and temporarily considering the EPC composite as a homogeneous continuous isotropic material, this paper explores a hyperelastic constitutive model for EPC through basic mechanical tests, curve fitting within a 95% confidence interval (Section 3), and model validation (Section 4). Finally, the developed hyperelastic model is applied into the failure analysis of ERS under longitudinal force (Section 5).

2. Hyperelastic constitutive

2.1. Derivation of the stress–strain relationship

A hyperelastic material is still an elastic material but its stress–strain relationship is nonlinear especially when the material undergoes large deformation. In hyperelastic constitutive, the stress–strain relationship is derived from the strain energy density function Φ based on the three strain invariants I_1, I_2, I_3, or principal stretch ratios λ_1, λ_2, λ_3 [16–36].

$$S = \frac{\partial \Phi}{\partial \boldsymbol{E}} \tag{1}$$

$$\Phi = \Phi(I_1, I_2, I_3) \text{ or } \Phi = \Phi(\lambda_1, \lambda_2, \lambda_3) \tag{2}$$

where $\boldsymbol{S}$ is the second Piola-Kirchhoff stress tensor, and $\boldsymbol{E}$ is the Green-Lagrangian strain tensor.

The strain invariants and principal stretch ratios are linked by the right Cauchy-Green deformation tensor $\boldsymbol{C}$ or the left Cauchy––Green deformation tensor $\boldsymbol{B}$.

$$\begin{cases} I_1 = tr(\boldsymbol{C}) = \lambda_1^2 + \lambda_2^2 + \lambda_3^2 \\ I_2 = \frac{1}{2}\left[(tr(\boldsymbol{C}))^2 - tr(\boldsymbol{C}^2)\right] = \lambda_1^2\lambda_2^2 + \lambda_2^2\lambda_3^2 + \lambda_3^2\lambda_1^2 \\ I_3 = det\boldsymbol{C} = J^2 = \lambda_1^2\lambda_2^2\lambda_3^2 \end{cases} \tag{3}$$

where $tr(*)$ is the trace function and J is the Jacobian determinant.

$\boldsymbol{E}$, $\boldsymbol{C}$ and $\boldsymbol{B}$ are derived from the deformation gradient tensor $\boldsymbol{F}$,

$$\begin{cases} E = \frac{1}{2}\left(F^T F - I\right) \\ C = F^T F \\ B = F F^T \end{cases} \tag{4}$$

where I is the identity tensor and

$$F = \begin{bmatrix} \lambda_1 & 0 & 0 \\ 0 & \lambda_2 & 0 \\ 0 & 0 & \lambda_3 \end{bmatrix} \tag{5}$$

In contrast to the second Piola–Kirchhoff stress tensor that relates forces and areas both in the reference configuration, the Cauchy stress tensor σ expresses the stress relative to the current configuration, and

$$\sigma = J^{-1} F S F^T \tag{6}$$

From observations in our previous experiments [5,15], the EPC, as a rubber-like material, is possibly incompressible and isotropic. Thus, to simplify the problem, the EPC is assumed to be incompressible and isotropic. With these assumptions, the developed model matches well with the test results. Therefore, for incompressible isotropic hyperelastic materials, a constitutive equation can be given [16]

$$\sigma = -pI + 2\frac{\partial \Phi}{\partial I_1}B - 2\frac{\partial \Phi}{\partial I_2}B^{-1} \tag{7}$$

where p is the indeterminate Lagrange multiplier that is associated with incompressibility. Additionally, the incompressibility assumption makes J equal 1, namely $\lambda_1\lambda_2\lambda_3 = 1$.

2.2. Candidate models

The candidate models considered in this paper are among the most popular ones including the Mooney-Rivlin models with 2, 3 and 5 parameters, respectively, the Ogden models with 1 and 2 terms, respectively, the Yeoh model with three parameters and the Arruda-Boyce model with 2 parameters. They are expressed as follows:

a. Mooney-Rivlin models:

1) with 2 parameters C_{10} and C_{10}:

$$\Phi_{MR2} = C_{10}(I_1 - 3) + C_{01}(I_2 - 3) \tag{8}$$

2) with 3 parameters C_{10} , C_{01} and C_{11}:

$$\Phi_{MR3} = C_{10}(I_1 - 3) + C_{01}(I_2 - 3) + C_{11}(I_1 - 3)(I_2 - 3) \tag{9}$$

3) with 5 parameters C_{10}, C_{01} , C_{11} , C_{20} and C_{02}:

$$\begin{aligned} \Phi_{MR5} = C_{10}(I_1 - 3) + C_{01}(I_2 - 3) + C_{11}(I_1 - 3) \\ (I_2 - 3) + C_{20}(I_1 - 3)^2 + C_{02}(I_2 - 3)^2 \end{aligned} \tag{10}$$

b. Ogden models with parameters μ_i and α_i

$$\Phi_{On} = \sum_{i=1}^{n} \frac{\mu_i}{\alpha_i}\left(\lambda_1^{\alpha_i} + \lambda_2^{\alpha_i} + \lambda_3^{\alpha_i} - 3\right) \tag{11}$$

where $n = 1, 2$;

c. Yeoh model with 3 parameters C_1, C_2 and C_3

$$\Phi_{Y3} = C_1(I_1 - 3) + C_2(I_1 - 3)^2 + C_3(I_1 - 3)^3 \tag{12}$$

Arruda-Boyce model with 2 parameters μ and λ_m

$$\Phi_{AB} = \mu \sum_{i=1}^{N} \frac{C_i}{\lambda_m^{2i-2}} \left(I_1^i - 3^i\right) \tag{13}$$

where $N = 5$, $C_1 = \frac{1}{2}$, $C_2 = \frac{1}{20}$, $C_3 = \frac{11}{1050}$, $C_4 = \frac{19}{7000}$, $C_5 = \frac{519}{673750}$.

The main task in the development of a hyperelastic model is to determine the parameters of a model function. Since the strain energy density function is based on strain invariants or principal stretch ratios, it is possible to fit the parameters with a few deformation modes in some basic and simple tests such as uniaxial tension or shear. Moreover, a hyperelastic model should operate satisfactorily in as many deformation modes as possible.

In this paper, uniaxial tension, planar tension and quadruple shear tests are conducted, where the first two are used for model development and the quadruple shear test is used for model validation.

3. Mechanical tests and model selection

3.1. Uniaxial tension tests and planar tension tests

The strain rate is possible to affect the test results [37–39]. But to simplify the problem, the strain rate is tentatively kept low with a crosshead velocity of 5 mm/min in both the uniaxial tension and the planar tension tests. This quite low strain rate is suitable for the failure analysis of ERS (see Section 5). All the tests are conducted in laboratory at a constant temperature of 20 ℃. Thus, the influence of temperature is also tentatively ignored. The effects of strain rate and temperature as well as their coupling on the EPC will be investigated in the near future.

The uniaxial tension test specimens are dumbbell-shaped, and tailored according to Type 1 in GB/T 528-2009 [40]. The test is performed on GOTECH AI-7000S testing machine and it is loaded until each specimen breaks. The loading situation and test results are shown in Figure 2(a) and Figure 2(b). As depicted in Figure 2(b), each specimen undergoes a relatively similar stress-strain path. This means that the tests are repeatable and that the mechanical property of EPC is stable. However, the final strength and final elongation when the specimens break vary considerably.

The specimens in the planar tension test are rectangular with dimensions of 80 mm × 100 mm × 2 mm. Each side along the stretch direction is assigned 30 mm as the clamping portion, cold bonded with metallic strips, and the middle 20 mm is used as the stretching portion, then the aspect ratio is 5 (100 mm divided by 20 mm). There is no standard dimension of specimens for the planar tension test. Duncan et al. [41] studied the influence of the aspect ratio of plane tensile specimens on test results, and recommended aspect ratios ranging from 4 to 10. The loading situation and test results in the current research are shown in Figure 2(c and d). Similar to the situation in the uniaxial tension tests, with similar stress-strain paths, the planar tension tests also demonstrate good repeatability. However, the final strength and final elongation when the specimens break vary considerably.

Wang et al. [15] found that when the shear strain of EPC or rubber strip reaches 120%, there should be material tear or interfacial debonding behaviour happening in the ERS. Thus, there is no need to develop a constitutive model matching the entire stress–strain curve where the engineering strain is up to 500%–700%. Furthermore, it seems difficult to obtain a uniform final strength or elongation in the uniaxial tension or planar tension tests. Therefore, the strain scope of interest could be limited to a smaller strain range, e.g. within 120%. In this work, to allow sufficient clearance, the strain scope of interest is selected to be in the range of 0–150%. As shown in
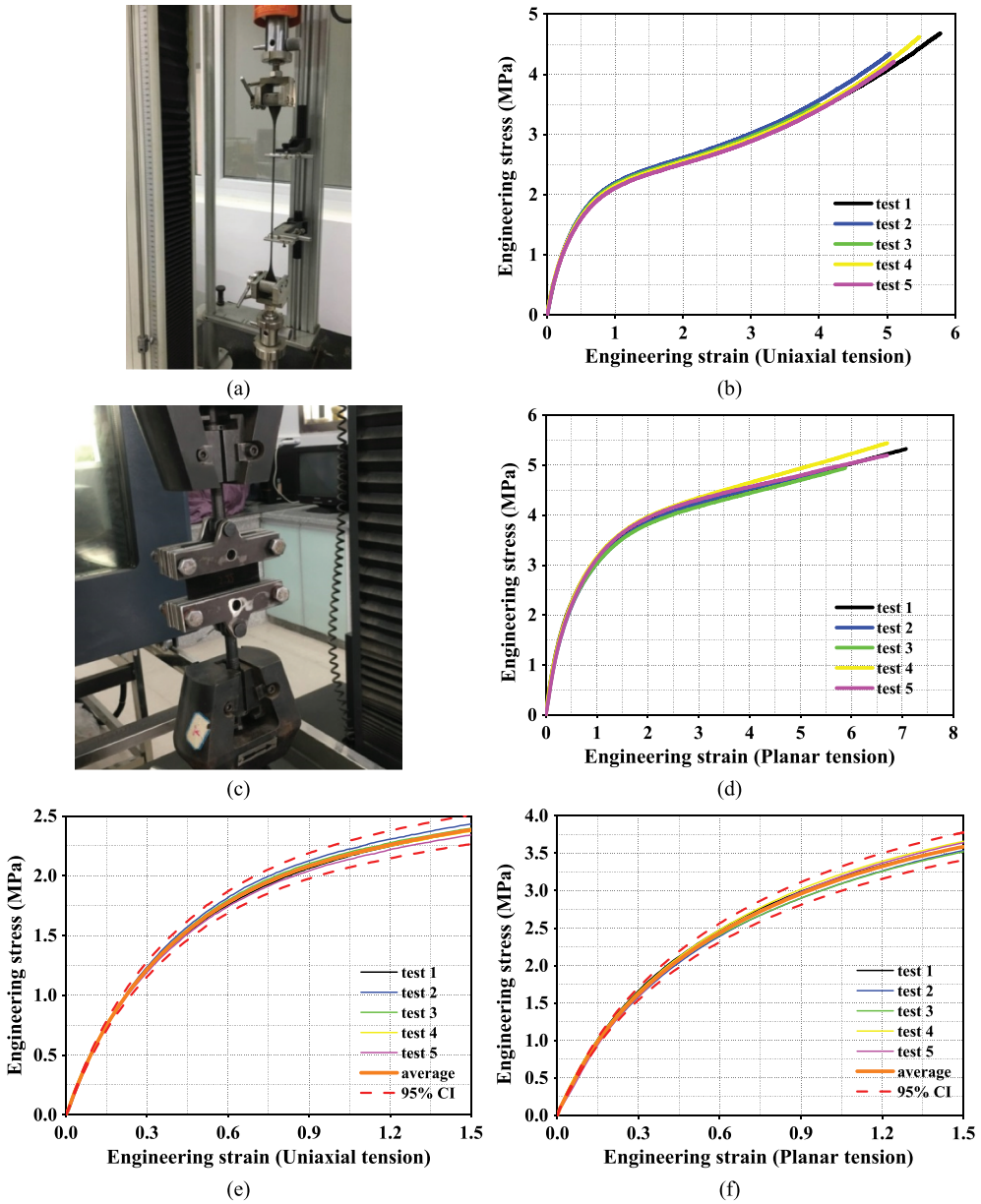
Figure 2. Uniaxial tension (UT) and planar tension (PT) tests: (a) UT test device; (b) UT test results; (c) PT test device; (d) PT test results; (e) UT test results within 150% engineering strain; (f) PT test results within 150% engineering strain. (CI-confidence interval).

Figure 2(e and f), the stress–strain curves are captured within the engineering strain range below 150%.

A 95% confidence interval is set in Figure 2(e and f). It can be seen that all the test results are guaranteed to be within the 95% confidence interval of the average values within the 150% engineering strain range. It should be kept in mind that the subsequently developed hyperelastic constitutive model based on these test results within 150% engineering strain range would be applicable only to the cases within the 150% engineering strain range, such as in the study on the failure analysis of ERS in Section 5.

3.2. Curve fitting

Based on the data measured in the uniaxial tension and the planar tension tests described above, a set of parameters for each model mentioned in Section 2, is determined by regression analysis. In curve fitting, the difference between the stress values of a measured curve and those derived from a model equation should be minimized to an acceptable level.

The normalized least squares fitting method is applied, as expressed in [42]:

$$\varepsilon_{norm} = \sum_{i=1}^{n} \left(\left(1 - \frac{\sigma_{ut,m}(i)}{\sigma_{ut,e}(i)}\right)^2 + \left(1 - \frac{\sigma_{pt,m}(i)}{\sigma_{pt,e}(i)}\right)^2 \right) \rightarrow \text{Minimum} \tag{14}$$

where ε_{norm} is the least-squares error, n is the number of measured data, $\sigma_{ut,m}$ and $\sigma_{pt,m}$ are the computed uniaxial tension stress and planar tension stress from a model equation respectively, and $\sigma_{ut,e}$ and $\sigma_{pt,e}$ are the averaged stress data in uniaxial tension tests and planar tension tests, respectively.

To make no bias towards uniaxial tension or planar tension tests, the data measured in the uniaxial tension tests should be treated with the same importance as that of the planar tension tests. Thus, no weight is put to neither of them.

The parameters and least-squares error for each model obtained from the curve fitting are listed in Table 1.

where Ogden4 represents the two-term Ogden model with 4 parameters, MR5 represents the Mooney-Rivlin model with 5 parameters, A-B represents the Arruda-Boyce model and so on.

In the regression analysis, nonlinear iterative calculation is necessary and different optimization algorithms, such as Levenberg-Marquard, Nelder-Mead, Powell, CG and COBYLA, are compared [43]. The curve fitting results could be slightly different when using different algorithms. The results with a smaller least-squares error would be selected on the basic condition that the error difference between the neighbouring iterations is less than 10^{-8}.

To make it clearer, the models with parameters in Table 1 are illustrated in Figure 3.

It can be seen from Table 1 and Figure 3 that, the two-term Ogden model with 4 parameters has the best fitting, followed by the Mooney-Rivlin model with 5 parameters. The Arruda-Boyce model is not shown in Figure 3 because its fitting result is of poor quality and unacceptable. In the review [20], all hyperelastic models are categorized into three types and the Arruda-Boyce model is a kind

Table 1. Parameters and least-squares errors obtained from curve fitting.

No.	Model	Parameters	Parameter value	ε_{norm}
1	Ogden4	μ_1	16.561 MPa	0.09434
		a_1	0.225	
		μ_2	−0.082 MPa	
		a_2	−3.585	
2	MR5	C_{10}	0.53982 MPa	0.17279
		C_{01}	0.44032 MPa	
		C_{20}	0.10673	
		C_{11}	−0.40297	
		C_{02}	0.26525	
3	MR3	C_{10}	0.39394 MPa	0.20425
		C_{01}	0.59633 MPa	
		C_{11}	−0.032945	
4	Ogden2	μ_1	705.896	0.87704
		a_1	0.006	
5	MR2	C_{10}	0.34013 MPa	2.63574
		C_{01}	0.54568 MPa	
6	Yeoh3	C_1	0.96302 MPa	5.19290
		C_2	−0.10117	
		C_3	0.0099733	
7	A-B	μ	1.46503 MPa	12.19282
		λ_m	24,433,637.029	
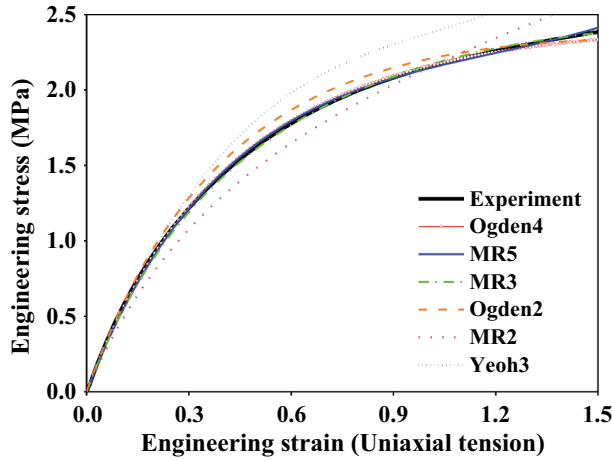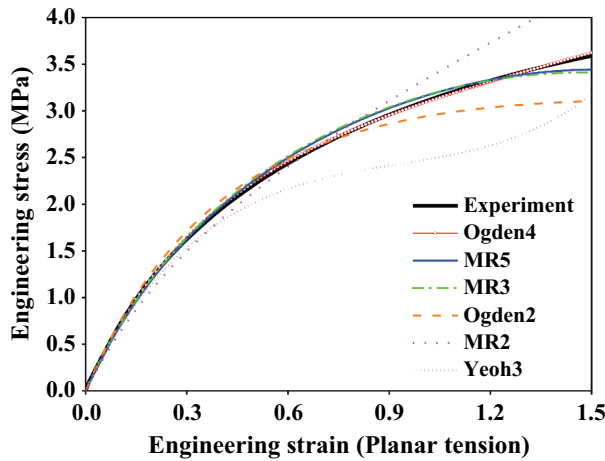
Figure 3. Curve fitting results: (a) uniaxial tension, and (b) planar tension.

of physically based model that associates the microscopic response of polymer chains in the network. However, EPC is some kind of composite rather than a single component. Therefore, it is difficult to simulate EPC with the Arruda-Boyce model, while the other phenomenological models would be more suitable.

Comparing the top five models, it can be found that, a higher order model gives a better fitting result. When taking the Ogden models as an example, the fitting result from 4 parameters (two-term) is better than that from 2 parameters (one-term). Also, for the Mooney-Rivlin models, the 5-parameter model is better than the 3- or 2-parameter model. This is not difficult to understand because, with more parameters, a model can express a larger set of curves, and eventually has the stronger ability to more closely approach the measured curves. However, it is worth mentioning that more parameters will entail higher computational cost.

From Figure 3, it can also be noticed that the fitting effect in Figure 3(a) is to some extent different from that in Figure 3(b). For the uniaxial tension test, many of the models can obtain quite good fitting results, but for the planar tension test, only the two-term Ogden model gets the perfect fitting. This is usually the exact difficulty encountered when developing a hyperelastic model in reality that it is easy to find a model operating perfectly in one deformation mode but it is always

difficult to make that model operate also satisfactorily in other deformation modes. The final model selection has to strike a balance among the fitting qualities of multifold deformation modes.

In view of the good fitting performance in both the uniaxial tension test and the planar tension test, the two-term Ogden model with 4 parameters, henceforth called Ogden4EPC, is selected as the most suitable hyperelastic model for EPC and brought into the next step: model validation.

4. Progressive model validation

4.1. Reproduction of the mechanical tests with the finite element method

In order to validate the material model Ogden4EPC, a finite element analysis (FEA) is conducted to simulate the responses under the uniaxial tension and the planar tension tests. Since the material model is developed based on the experimental results, the model should be suitable in FEA to simulate the tests. Moreover, a quadruple shear test is performed and also simulated in FEA to verify the predictions with the model. This is the progressive validation strategy in this section.

Figure 4 shows the FEA models developed in ANSYS and the simulation results. For the uniaxial tension (see Figure 4(a)), the red parts are the clamped portion, and one side is rigidly fixed without displacement in three directions while a distributed force is applied to the opposite side to stretch the specimen. Only the deformation of the middle portion with a length of 25 mm is calculated for engineering strain.

Similarly, for the planar tension (see Figure 4(b)), the purple parts are clamped, and only the green part in the middle of the specimen is deformed under the pulling load. The FEA results are shown in Figure 4(c). From Figure 4(c), compared with the test results, it can be concluded that the simulation results reproduce the test results well, and also match the model equation curves well.

4.2. Additional quadruple shear test and its reproduction

Figure 5 describes the quadruple shear test and its simulation in ANSYS.

In Figure 5(b), each test is carried out according to GB/T 12830-2008 [44]. Four blocks of EPC with dimensions of 25 mm × 20 mm × 5 mm are formed when the liquid EPC solidified in the mould that had been painted inside with adhesive that is usually used to enhance the bond between EPC and rail. The two inside metal strips are pulled at a low strain rate with a crosshead velocity of 5 mm/min until the EPC tears itself or detaches from the metal strips.

Similar to the tension tests above, the shear tests could also only get similar stress-strain paths but vary considerably at the final strength and final elongation (see Figure 5(c)). When the strain goes up to high values, approximately above 150%, the curves become quite divergent. With the same method as that used for the uniaxial tension and the planar tension tests, the stress–strain curves obtained from the quadruple shear test are also captured within the 150% engineering strain (see Figure 5(d)).

In the simulation of the quadruple shear test (see Figure 5(e)), the lower inside steel plate is constrained with no displacement in three directions, while the upper inside steel plate is pulled upwards gradually with the constraint of $U_x = U_z = 0$. It can be seen from the simulation result that, as demonstrated in Figure 5(F), although the simulation results do not completely coincide with the test results, the calculated stress–strain curve is still well enclosed in the 95% confidence interval within the 150% engineering strain range.

With the good agreement between simulation and experimental results for uniaxial tension, planar tension and quadruple shear tests, it is concluded that the constitutive model Ogden4EPC can successfully describe the hyperelasticity of EPC. Subsequently, this hyperelastic model Ogden4EPC will be applied into the failure analysis of ERS to study the influence of the hyper-elasticity of EPC on the damage development in ERS.
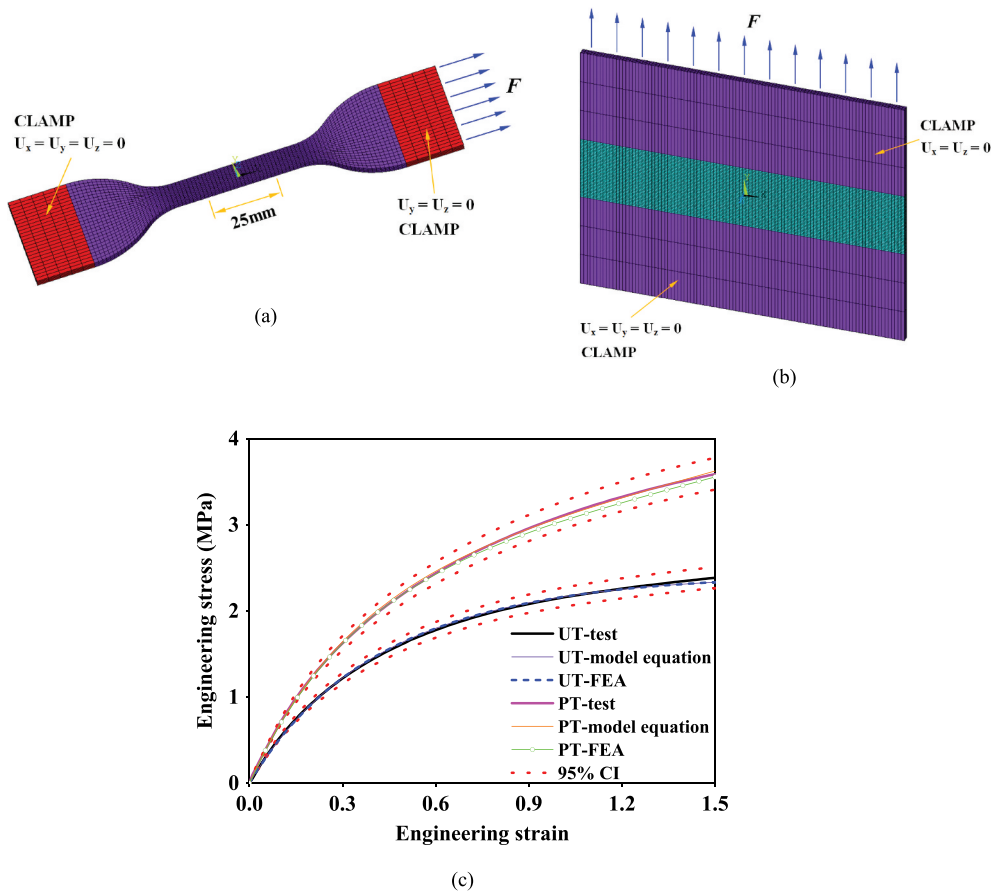
Figure 4. FEA models and simulation results in model validation: (a) uniaxial tension; (b) planar tension; (c) simulation results in FEA. (UT-uniaxial tension; PT-planar tension; CI-confidence interval).

5. Application in failure analysis of ERS under longitudinal force

5.1. Experimental investigation on damage development in ERS

ERS is becoming widely used all over the world. Despite the many advantages of ERS, cracks and debondings can often be found at many operating lines, as shown in Figure 6. Cracks can happen at the interfaces between components and can also occur in EPC itself. Debondings are a more detrimental form of damages at the interfaces where cracks are fully developed.

To better understand ERS and its damage development, a laboratory experiment was designed to explore the initiation and growth of damage in ERS under longitudinal force [15]. In the experiment, two 600 mm full ERS specimens were prepared. Each of them contained the main characteristics of ERS and was pushed longitudinally via a load cell. The rail displacement was measured by displacement metres and the deformation of EPC was captured by cameras from top and side views using the method of particle image velocimetry & digital image correlation (PIV-DIC) [45,46], as shown in Figure 7.

In the experiment, it was found that the longitudinal stiffness of ERS is decreasing as the longitudinal force increases. The stiffness decrease involves two factors. One is the material nonlinearity (most probably hyperelasticity in this case) and the other is the development of cracks and debondings in ERS.

It was found that the places where large shear deformation underwent were the most vulnerable places, such as the rubber strip right under the rail. It is most probably that debonding first occurred
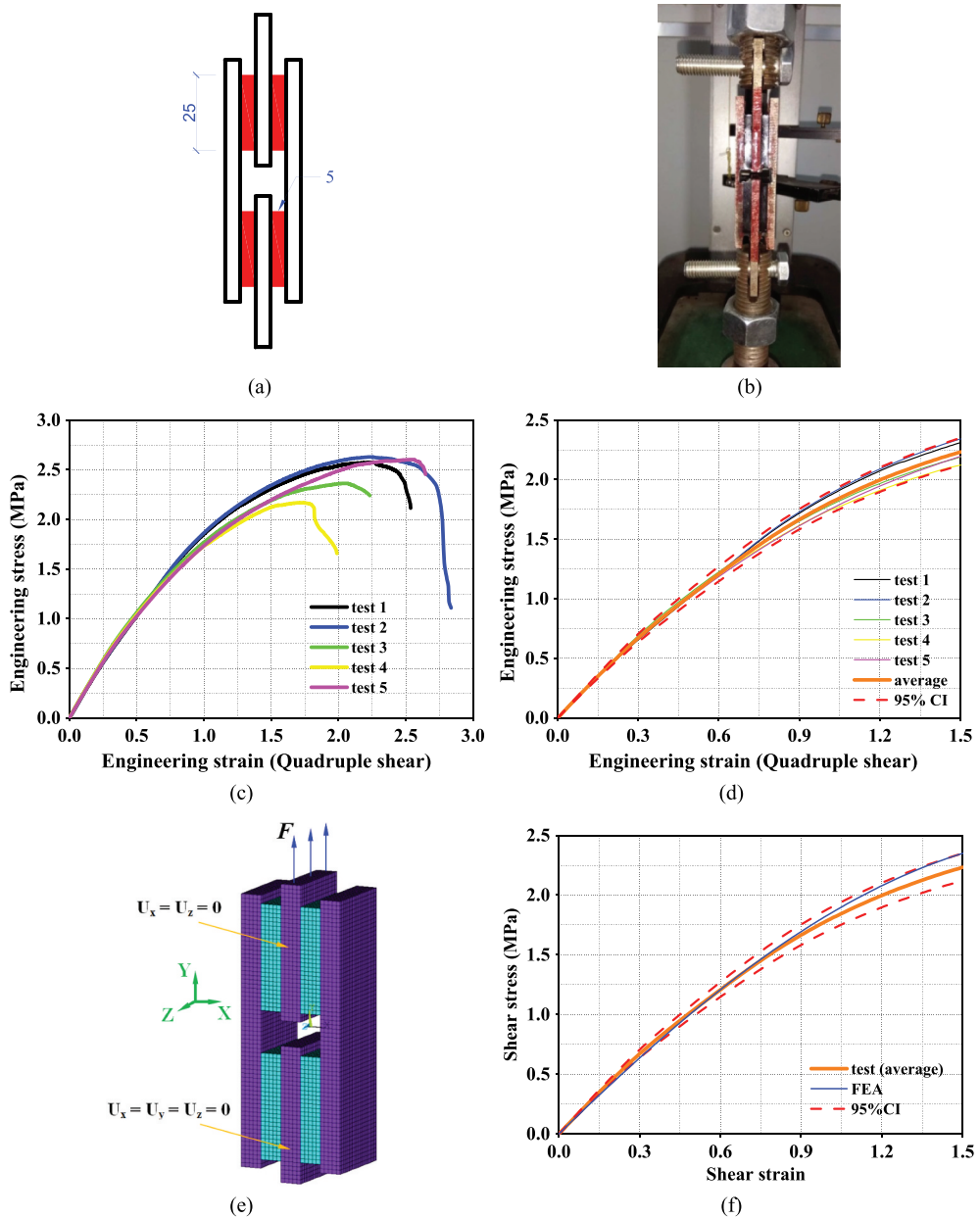
Figure 5. Quadruple test and simulation: (a) dimensions of specimen (mm); (b) test situation; (c) test results over the full strain range; (d) test results within 150% engineering strain; (e) FEA model of the quadruple shear test; (f) simulation result of quadruple shear.

between the rubber strip and concrete groove, then came to the rail foot at the interface between EPC and the rail, and then the interface between EPC and the concrete groove.

Figure 8 shows the three debondings observed in the experiments.

In the previous simulations in [15], with a qualitative analysis, it was found that, at early stage, at the place right under the rail, the rubber strip took the largest shear deformation and shear stress, thus was the most vulnerable place. If the 1st debonding was pre-established, namely the rubber strip was assumed to have debonded from the concrete groove before, then the interface between

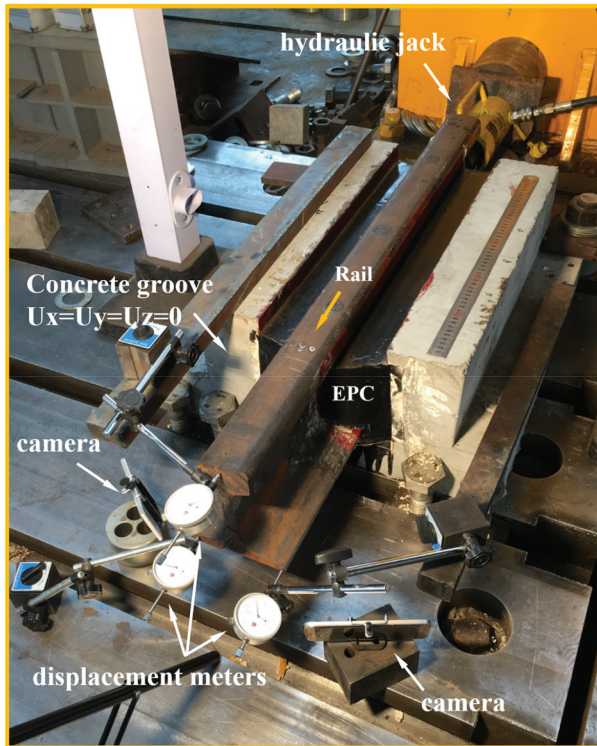**Figure 6.** Cracks and debondings observed at operating lines.

Figure 7. Experiment in the failure analysis of ERS under longitudinal force.

rail and EPC at the rail foot would be the most vulnerable place where it had the largest shear deformation and shear stress. After that, the interface between EPC and concrete groove became vulnerable. Therefore, roughly, the three debondings were confirmed in the previous simulations.

However, in the previous simulations in [15], the EPC was considered as a linear elastic material that is based on an infinitesimal strain assumption. When the deformation is large, such as with
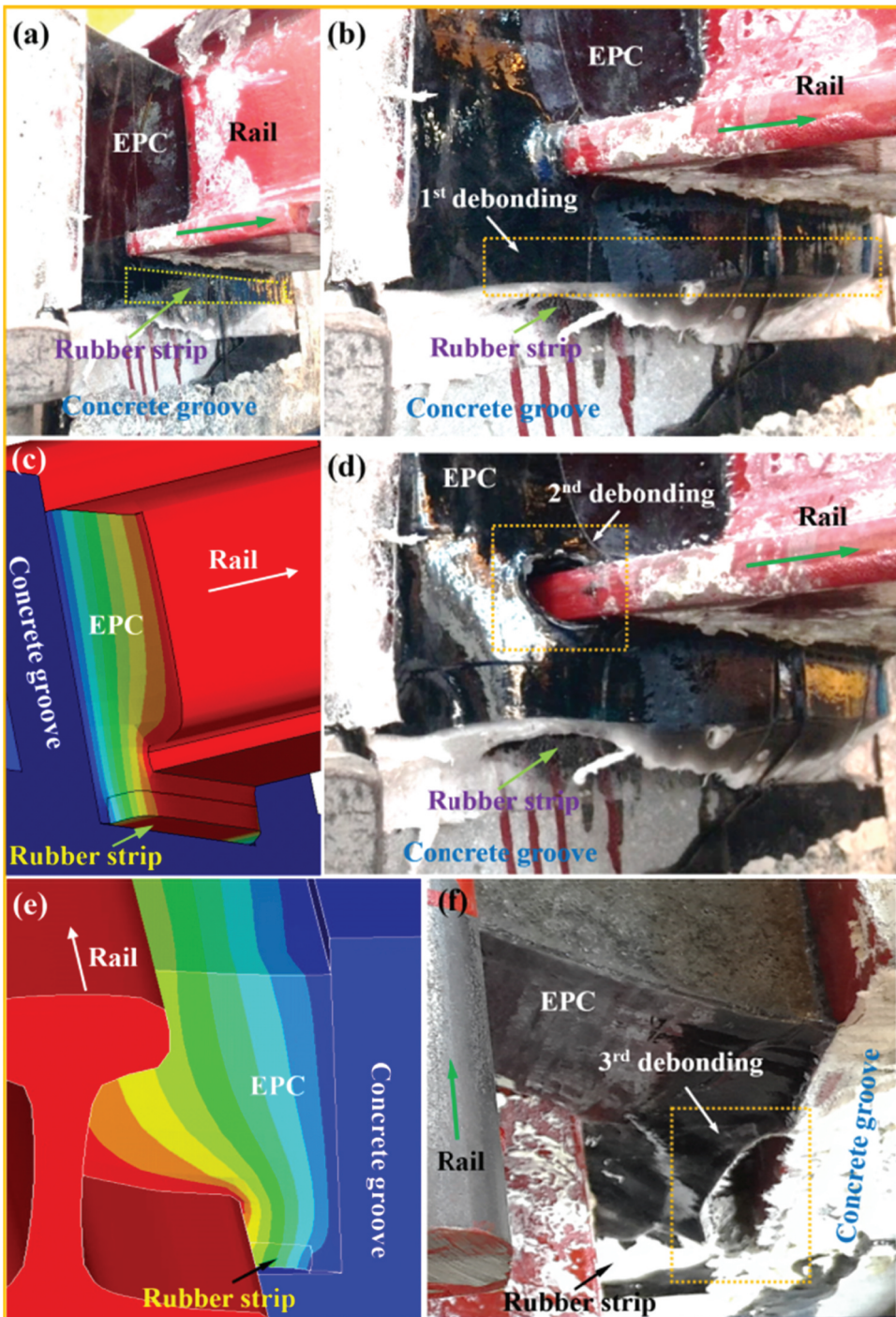
Figure 8. Debondings in ERS observed in the experiments. (a) initial state; (b) the 1st debonding at the interface between rubber strip and concrete groove; (c) schematic diagram of the 1st debonding at the rail free end; (d) the 2nd debonding at the interface between the rail foot and EPC; (e) schematic diagram of the 1st debonding at the rail push end; (f) the 3rd debonding at the interface between the EPC and the concrete groove.

a strain more than 20%, the results would be not accurate or reliable any more. The developed hyperelastic model in this work will overcome this limitation.

In the following subsections, the hyperelasticity of EPC will be fully considered to further explore the debonding behaviours in ERS under longitudinal force. Moreover, a preliminary trial simulation of crack propagation in ERS will be conducted to obtain more details of the failure at the debonding interface between the rail and EPC at the rail foot.

5.2. Debonding behaviour in ERS under longitudinal force

With the selected hyperelastic model Ogden4EPC, the simulation of stiffness decrease of ERS under longitudinal force is expected to give a more realistic result than the previous simulations in [15]. The finite element model is updated by applying the hyperelasticity of EPC, as shown in Figure 9.

In Figure 9, the rail is pushed by the longitudinal force F and the concrete groove is fixed at its bottom to a rigid floor. In the finite element model, the 8-node solid element type is employed. The dimensions of the smallest element are 3.2 mm × 3.3 mm × 20.0 mm (in the x, y and z directions, respectively). This fine mesh for EPC lies in the vicinity of the rail foot and the concrete groove corners, where relatively large shear strains were found in our previous experimental study [15]. The mesh size is determined through trial simulations. Coarse mesh will lead to inaccurate results, while too fine mesh will cause a high computation cost. The current mesh size is a compromise of these two considerations.

For the three debondings in Figure 8, in the FEA model, they are considered as three pairs of contact interfaces coupled with friction, as shown in Figure 9(b). A penalty-based contact algorithm is employed to calculate the contact force that is proportional to the penetrations [47,48]. The debonding length L_1 at the rail foot is 30 mm and the debonding length L_2 at the concrete groove corner is 81 mm. For the other interfaces without any pre-established debondings, the components share nodes with their counterpart components, namely they have no relative displacement at the interfaces [47,49].

The following simulations are performed to study the influences of different treatments of the model in reproducing the experimental results: the treatment of EPC material as elastic or hyperelastic, and then the debonding behaviours with different damage levels. In total, 7 cases are considered as described in Table 2.

The material parameters of the other components are all the same in the 7 cases, as listed in Table 3.

The numerical and experimental results are shown in Figure 10.

It can be seen from Figure 10 that, when the EPC is presumed to be linear elastic, the force-rail displacement curve obtained from the simulation is almost linear (see the blue dot line in Case 1, when the displacement is larger than 5 mm, the result is probably not reliable), while when the hyperelastic model Ogden4EPC is employed for EPC, the simulation is able to give 'logarithmic shape' lines, namely bending slightly (see the other cases except Case 1). These 'logarithmic shape' lines can better represent the experimental results, except for the different degrees of the bending. Therefore, the application of hyperelastic model Ogden4EPC makes the simulation better than that when EPC is considered as linear elastic material.

The bending of force-displacement curves means the longitudinal stiffness of ERS is decreasing. The stiffness decrease involves not only the cracks and debondings in ERS but also the nonlinearity of EPC (and rubber strip) which is shown from the numerical simulation. Furthermore, from Case 2, via Case 3 and 4, to Case 7 (see the solid symbol lines in Figure 10), the bending becomes more and more considerable. This can be explained that, with more pre-established debondings (see Figures 8 and 9), the deformation would be larger, and correspondingly the effect of hyperelasticity is more obvious.

The simulations in Case 2, Case 3, Case 4 and Case 7 are still unable to perfectly represent the experimental results. However, some conclusions can be drawn from them. Case 2 does not
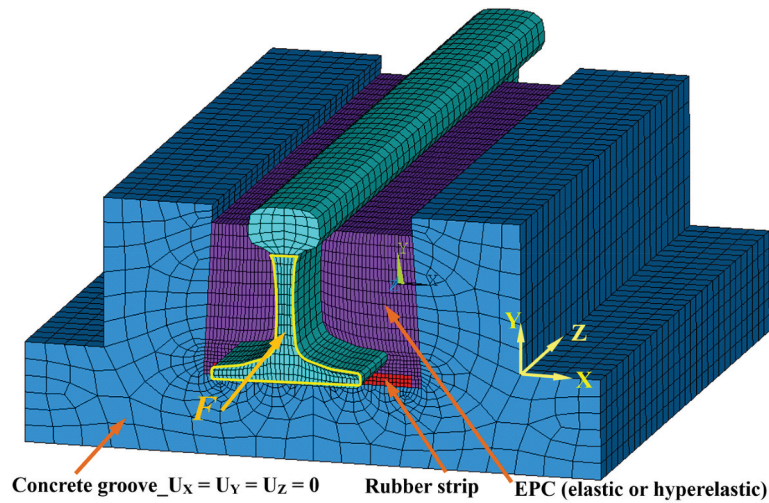
(a) load and constraint applied in the FEA model
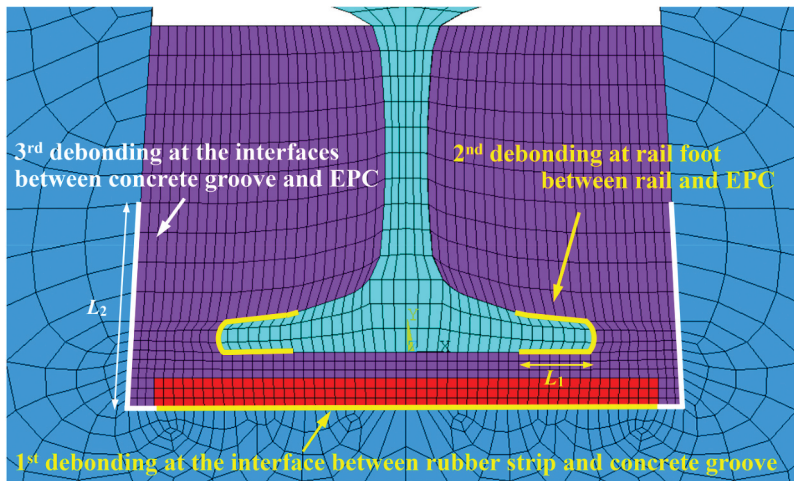
(b) considerations of debondings at the interfaces

Figure 9. FEA model and considerations of debondings in the failure analysis of ERS under longitudinal force.

consider any pre-established debonding nor any crack or debonding during the loading process. The difference between the simulation in Case 2 and the experimental result (1# or 2# Specimen) is most probably due to the cracks and debondings those occur in ERS during the loading process. The cracks and debondings can happen at the interface between the rubber strip and the concrete groove, the interface between the EPC and the concrete groove, as well as the interface between the EPC and the rail. In Case 3, Case 4 and Case 7, pre-established debondings are considered (see Tables 2 and 3). The intersections between the three lines (orange, pink and cyan lines) in these three cases and the experimental lines (black and red lines with hollow symbols), at the rail displacement of about 8 mm, 12 mm and 26 mm, can be explained as three critical states. For example, when the rail displacement is less than about 8 mm, the experimental lines are between the green line and the orange line, thus the (1st) debonding between the rubber strip and concrete groove is probably happening during this process. Similarly, when the rail displacement reaches about 12 mm, the debonding level in the experiment could be close to that defined in Case 4, where

Table 2. Descriptions of the 7 case studies.

Case	Descriptions
1	• No debonding between any components; • EPC is presumed as linear material with an elastic modulus of 6 MPa(determined by trial simulations in [15]);
2	• No debonding between any components; • Hyperelastic model Ogden4EPC is applied to EPC;
3	• Rubber strip is not glued to the concrete groove but friction exists between them with a friction coefficient of 0.8 [50,51]; • No debonding between the other components; • Hyperelastic model Ogden4EPC is applied to EPC;
4	• Rubber strip is not glued to the concrete groove but friction exists between them with a friction coefficient of 0.8; • EPC is not glued to the rail at the rail foot but friction exists between them with a friction coefficient of 0.64 [50,52]; $(L_1 = 30$ mm) • No debonding between the other components; • Hyperelastic model Ogden4EPC is applied to EPC.
5	• EPC is not glued to the rail at the rail foot but friction exists between them with a friction coefficient of 0.64 [50,52]; $(L_1 = 30$ mm) • No debonding between the other components; • Hyperelastic model Ogden4EPC is applied to EPC.
6	• EPC is not glued to the concrete groove at the concrete groove corners but friction exists between them with a friction coefficient of 0.8; $(L_2 = 76$ mm) • No debonding between the other components; • Hyperelastic model Ogden4EPC is applied to EPC.
7	• Rubber strip is not glued to the concrete groove but friction exists between them with a friction coefficient of 0.8; • EPC is not glued to the rail at the rail foot but friction exists between them with a friction coefficient of 0.64; • EPC is not glued to the concrete groove at the concrete groove corners but friction exists between them with a friction coefficient of 0.8; $(L_2 = 76$ mm) • No debonding between the other components; • Hyperelastic model Ogden4EPC is applied to EPC.

Table 3. Material properties of the components in ERS.

Components		Linear/nonlinear	Elastic modulus (MPa)	Poisson's ratio	Density (kg/m^3)	Debonding considerations
EPC	Case 1	Linear	6	0.499	1000	No debonding
	Case 2	Ogden4EPC	/	0.499	1000	No debonding
	Case 3	Ogden4EPC	/	0.499	1000	1st debonding
	Case 4	Ogden4EPC	/	0.499	1000	1st + 2nd debonding
	Case 5	Ogden4EPC	/	0.499	1000	2nd debonding
	Case 6	Ogden4EPC	/	0.499	1000	3rd debonding
	Case 7	Ogden4EPC	/	0.499	1000	1st+2nd+3rd debonding
Rail		Linear	2.06e5	0.3	7800	/
Rubber strip		Linear	0.7	0.45	600	/
Concrete groove		Linear	3.6e4	0.2	2400	/

the 1st and 2nd debondings are both happened. When the rail displacement reaches about 26 mm, the debonding level in the experiment could be close to that defined in Case 7, where all the three debondings are happened. With more and accurate pre-established debondings, the debonding process can be acquired and the debonding behaviour in ERS can be better understood. Comparing the Cases 2, 3, 5 and 6, the contribution of each kind of debonding to the rail longitudinal displacement is clear. The 1st debonding, at the interface between the rubber strip and concrete groove, contributes the most, while the other two debondings, if without the 1st debonding, contribute much less. This is because the most vulnerable part of ERS under longitudinal force is the rubber strip that sustains the largest shear deformation among all parts.
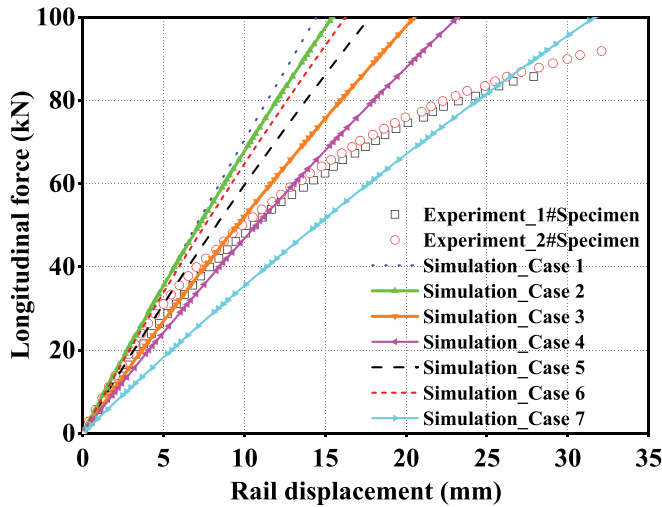
Figure 10. Force-rail displacement curves: simulation and experimental results.

5.3. Preliminary simulation of crack propagation in ERS

A debonding is actually a more developed state of cracks at an interface. To get more details of a debonding at an interface, in this subsection, a preliminary simulation of crack propagation is conducted.

Crack propagation in ERS is very complex because there are multiple types of materials and vulnerable structural interfaces in ERS. In this preliminary simulation, the focus is on the EPC itself, especially at the interface between the rail and EPC at the rail foot. The other components are assumed to be with no failure.

An FE model similar to that in Figure 9(a) but with a much finer mesh at the rail foot and the groove corner is created, as shown in Figure 11.

In Figure 11, the rail is gradually pushed with a longitudinal force *F*, while the concrete groove is rigidly fixed to the ground. To get accurate results, the mesh should be sufficiently fine. The dimensions of the smallest element are 0.6 mm × 0.7 mm × 12.5 mm (in the x, y and z directions, respectively) in this trial simulation for the sake of computation time. The time step is 8.74×10^{-8} s.

The model Ogden4EPC is applied to EPC thus the hyperelasticity can be fully considered. The material properties of the other components are the same as those listed in Table 2.

The failure criterion is defined as

$$T \geq 2.0 \text{MPa} \tag{15}$$

where *T* is the maximal shear stress.

The value 2.0 MPa is approximately determined through the observations in the quadruple shear test in Figure 5. When the shear stress is greater than 2.0 MPa, some minor failures could be observed in the test.

Once the failure criterion is satisfied, the element will be deleted from the calculation. Through this, the crack development can be determined. The crack propagation path in this preliminary simulation is shown in Figure 12.

In Figure 12, the crack initiates at the rail foot tip and develops along the directions of ③ and ④. However, according to the appearance of the 2nd debonding in Figure 8c, the crack in the experiment is found to initiate at the rail foot corner and propagate along the directions of ① and ②. This disagreement indicates that the 2nd debonding in the experiment is probably not caused by the failure of EPC but the failure of the adhesive at the interface between the
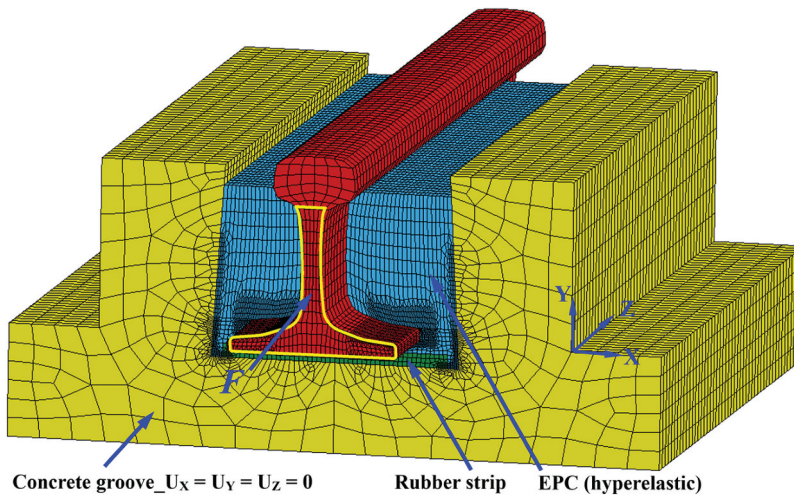
Figure 11. Much finer mesh at the rail foot and groove corner for a trial simulation of crack propagation.
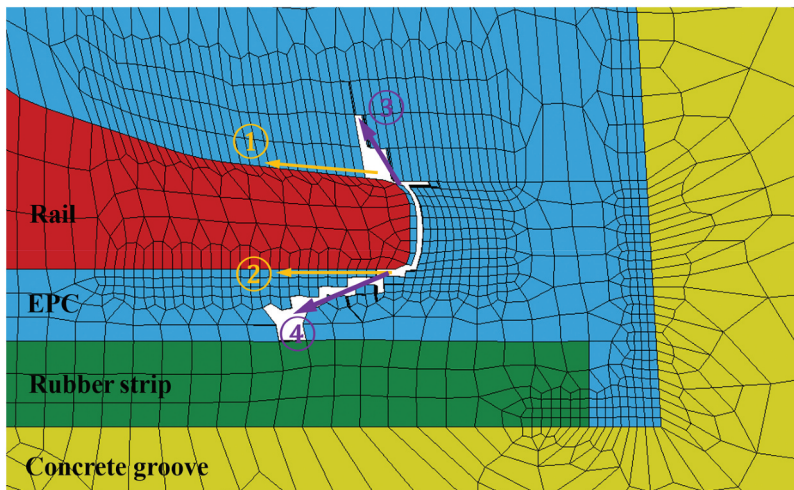

Figure 12. Crack propagation in EPC in this preliminary simulation.

EPC and the rail. Because if there is only failure in EPC, the crack will not develop along the interface between the rail and EPC but instead develops in the EPC itself, as shown in Figure 12.

The following observations in the experiments confirm this conclusion.

As shown in Figure 13, there is no or negligible residual EPC at the rail foot surface when the 2nd debonding happens, meaning debonding at the interface rather than EPC itself. Thus, at the interface between the rail and EPC, it is most probably that the (2nd) debonding is caused by the failure of the adhesive.

The crack propagation in the longitudinal direction is shown in Figure 14.

It can be seen from the Figure 14(a) that, the shear stress is generally quite uniform along the longitudinal direction at the state right before the crack appears. It indicates that the load transferred from the rail is quite uniform and then the shear deformation of EPC at the rail foot is also quite uniform along the rail. However, it shows from the Figure 14(b–d) that the crack starts from the rail push end and extends gradually to the rail free end. This crack propagation in the longitudinal
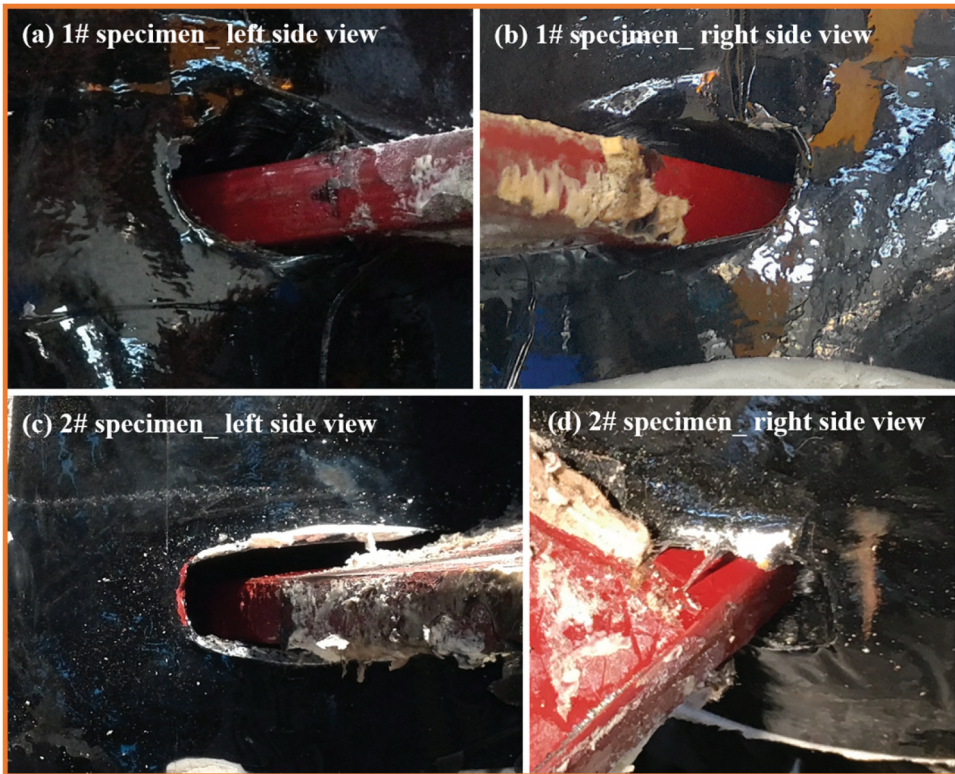
Figure 13. No or negligible residual EPC at the rail foot surface when the 2nd debonding happens.
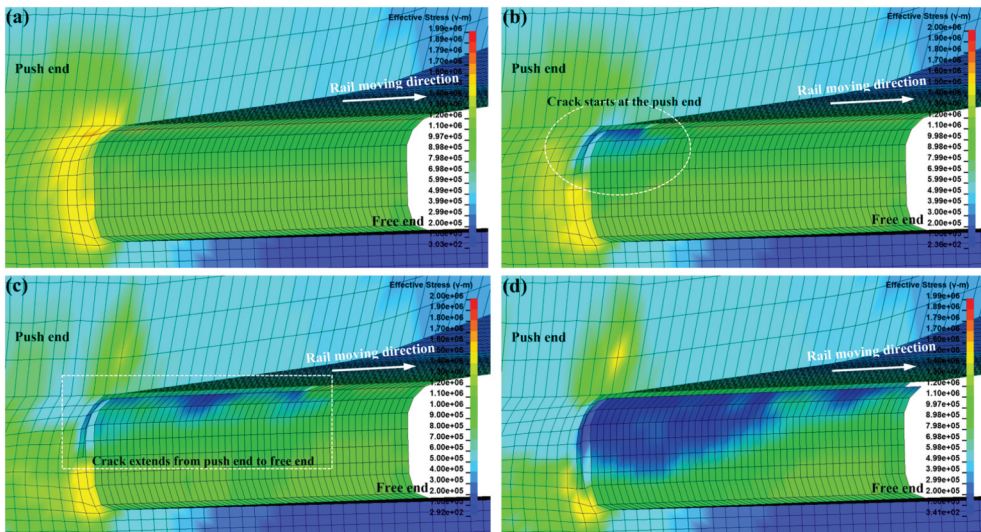

Figure 14. Crack propagation in longitudinal direction. (a) state right before crack appears; (b) crack starts at the rail push end; (c) crack extends from the rail push end to the rail free end; (d) crack extends thoroughly in the longitudinal direction.

direction in Figure 14 does not violate the observations in Figures 8(f) and 13, but it still needs to be further confirmed in future work when a proper failure detection method is available.

Considering the discrepancy between the experimental and numerical results, some conclusions can be made on the basis of the preliminary simulation. Firstly, the failure criterion is too simple to fully present the real failure scenario of a hyperelastic material [53,54]. A more reasonable failure criterion will be investigated in the future research. Second, the trial value (2.0 MPa) in the failure criterion may be not accurate. To solve this problem, more material tests shall be conducted to get the accurate strengths of the materials. Thirdly, the interfaces should be better considered [55,56]. In the current simulations, the interfaces are modelled as two components with shared nodes, namely the adhesives used to glue the interfaces are not considered. This disables the model to consider the failure due to the failures of the adhesive.

Thus, in future research, a more complete finite element model shall be developed. In the new model, not only the material nonlinearity but also the development of cracks and debondings at interfaces shall be fully considered. A more reasonable failure criterion should be employed. To this end, material tests shall be conducted to get the accurate strengths of EPC, rubber strip and especially the adhesives at the interfaces. Thus, the development of cracks and debondings in ERS can be better simulated.

6. Conclusions

EPC is the key component in ERS to realize non-fastener continuous homogeneous support of rails. Knowing more about the mechanical properties of EPC is essential to understand the special constraint mechanism of rails in ERS. Thus, a hyperelastic model Ogden4EPC is developed based on the two-term Ogden model with 4 parameters to explore the large deformation behaviour in the failure process of ERS.

As a typical engineering material, EPC shows a similar stress-strain path under given load condition with variability. It is shown that with the Ogden4EPC constitutive model this uncertainty is successfully covered within a 95% confidence interval for all the physical test results and numerical simulations of the uniaxial tension, planar tension and quadruple shear within the 150% engineering strain range.

In the failure analysis of ERS under longitudinal force, the application of the hyperelastic model Ogden4EPC results in better simulation result than that when linear elasticity is assumed for the EPC. With larger deformation, the effect of hyperelasticity is more obvious. With more pre-established debondings, the debonding behaviour in ERS can be better understood.

With a preliminary simulation of crack propagation in EPC at the rail foot, and the observations in the experiments, it is found that the 2nd debonding is probably not caused by the failure of EPC but the failure of the adhesive at the interface between the EPC and the rail.

In future work, more material tests shall be conducted to get the accurate strengths of EPC, rubber strip and especially the adhesives at the interfaces. A more reasonable failure criterion shall be established and the interface layer shall be fully considered. Thus, the bond-slip behaviour can be better simulated, the cracks and debondings are possible to be better reproduced with a more complete model, and then the damage development in ERS under longitudinal force can be better understood.

Acknowledgements

Disclosure statement

No potential conflict of interest was reported by the author(s).

ORCID

Li Wang http://orcid.org/0000-0001-7244-803X
Ping Wang http://orcid.org/0000-0002-2088-9279

References

[1] Edilon Sedra BV. *Brochures from edilon)(sedra* [EB/OL] [2022 Aug04]. Available from: https://www.edilonse dra.com/downloads/.
[2] Ahrens P, Dreger F, Giglmaier R, et al. Handbook track greening-design-implementation-maintenance. Berlin: Eurail Press; 2016.
[3] Houwen G, Kerkhoven P, Koteris S. Polymer composition, method for applying such composition and use of such composition in railway track structures. Patent No.: US 8,946,370 B2; 2015. https://patents.google.com/patent/US8946370B2/en
[4] Wang P, Wang L, Chen R, et al. Overview and Outlook on railway track stiffness measurement. J Mod Transp. 2016;24(2):89–102. DOI:10.1007/s40534-016-0104-8.
[5] Wang L, Xiao J, Wang Q, et al. Reasonable track stiffness of embedded rail structure used in metro. J Cent South Univ (Sci Technol). 2018;49(7):1831–1837.
[6] Sainz-Aja J, Carrascal I, Ferreño D, et al. Influence of the operational conditions on static and dynamic stiffness of rail pads. Mech Mater. 2020;148:103505.
[7] Vanlier S. The vibro-acoustic modelling of slab track with embedded rails. J Sound Vibr. 2000;231(3):805–817.
[8] Markine V, De Man A, Jovanovic S, et al. Modelling and optimization of an embedded rail structure. Rail Int. 2000;31(7):15–23.
[9] Major Z. A method for the numerical modelling of embedded rails and determining parameters to be optimized. Acta Tech Jaurinensis. 2016;9(1):16–28.
[10] De Man A. DYNATRACK: dynamic behaviour of railway track. Delft: Delft University of Technology; 2002.
[11] Zhao Y, Li X, Lv Q, et al. Measuring, modelling and optimising an embedded rail track. Appl Acoust. 2017;116:70–81.
[12] Han J, He Y, Xiao X, et al. Effect of control measures on wheel/rail noise when the vehicle curves. Appl Sci. 2017;7(11):1144. DOI:10.3390/app7111144.
[13] Yang Z, Zhang P, Wang L .Wheel-rail impact at an insulated rail joint in an embedded rail system. Eng Struct. 2021;246:113026. DOI:10.1016/j.engstruct.2021.113535.
[14] Stančík V, Ryjáček P, Vokáč M. Thermal and load rate-dependent interaction between embedded rail system and bridge. Proc Inst Mech Eng F J Rail Rapid Transit. 2019;233(3):326–336.
[15] Wang L, Wang P, Chen R, et al. Experimental and numerical investigation of damage development in embedded rail system under longitudinal force. Eng Fail Anal. 2020;114:104590.
[16] Holzapfel G. Nonlinear solid mechanics-a continuum approach for engineering. London: John Wiley & Sons, LTD; 2000.
[17] Truesdell C, Noll W. The non-linear field theories of mechanics. 3rd ed. Berlin: Springer; 2004.
[18] Nam-Ho K. Introduction to nonlinear finite element analysis. New York: Springer; 2015.
[19] Boyce M, Arruda E. Constitutive models of rubber elasticity: a review. Rubber Chem Technol. 2000;73(3):504–523.
[20] Marckmann G, Verron E. Comparison of hyperelastic models for rubber-like materials. Rubber Chem Technol Am Chem Soc. 2006;79(5):835–858.
[21] Beda T. Modeling hyperelastic behaviour of rubber: a novel invariant-based and a review of constitutive models. J Polym Sci B Polym Phys. 2007;45(13):1713–1732.
[22] Ali A, Hosseini M, Sahari B. A review of constitutive models for rubber-like materials. Am J Eng Appl Sci. 2010;3(1):232–239.
[23] Beda T. An approach for hyperelastic model-building and parameters estimation a review of constitutive models. Eur Polym J. 2014;50:97–108.
[24] Lancker B, Corte W, Belis J. Calibration of hyperelastic material models for structural silicone and hybrid polymer adhesives for the application of bonded glass. Constr Build Mater. 2020;254:119204.
[25] Mooney M. A theory of large elastic deformation. J Appl Phys. 1940;11(9):582–592.
[26] Rivlin R. Large elastic deformations of isotropic materials - I. Fundam Concepts Philos Trans R Soc A. 1948;240(822):459–490.
[27] Rivlin R. Large elastic deformations of isotropic materials - IV. Further developments of the general theory. Philos Trans R Soc A. 1948;241(835):379–397.
[28] Rivlin R, Saunders DW. Large elastic deformations of isotropic materials - VII. Experiments on the deformation of rubber. Philos Trans R Soc A. 1951;243(865):251–288.

[29] Ogden R. Large deformation isotropic elasticity - on the correlation of theory and experiment for incompressible rubberlike solids. Proc R Soc London Ser A Math Phys. 1972;326(1567):565–584.

[30] Yeoh O. Characterization of elastic properties of carbon-black-filled rubber vulcanizates. Rubber Chem Technol. 1990;63(5):792–805.

[31] Arruda E, Boyce M. A three-dimensional constitutive model for the large stretch behaviour of rubber elastic materials. J Mech Phys Solids. 1993;41(2):389–412.

[32] Montella G, Calabrese A, Serino G. Mechanical characterization of a tire derived material: experiments, hyperelastic modeling and numerical validation. Constr Build Mater. 2014;66:336–347.

[33] Gao J, Yang X, Guo Q, et al. Hyperelastic mechanical properties of chopped aramid fiber-reinforced rubber composite under finite strain. Compos Struct. 2020;243:112187.

[34] Valanis K, Landel R. The strain-energy function of a hyperelastic material in terms of the extension ratios. J Appl Phys. 1967;38(7):2997–3002.

[35] Rivlin R. The Valanis-Landel strain-energy function. J Elast. 2003;73(1–3):291–297.

[36] Rivlin R. The relation between the Valanis–Landel and classical strain-energy functions. Int J Non Linear Mech. 2006;41(1):141–145.

[37] Guo H, Guo W, Amirkhizi A. Constitutive modeling of the tensile and compressive deformation behaviour of polyurea over a wide range of strain rates. Constr Build Mater. 2017;150:851–859.

[38] Roland C. Mechanical behaviour of rubber at high strain rates. Rubber Chem Technol. 2006;79(3):429–459.

[39] Jerrams S, Kaya M, Soon K. The effects of strain rate and hardness on the material constants of nitrile rubbers. Mater Des. 1998;19(4):157–167.

[40] GB/T 528. 2009. Rubber, vulcanized or thermoplastic - determination of tensile stress-strain properties.

[41] Duncan B, Maxwell A, Crocker L, et al. Verification of hyperelastic test methods. NPL Report CMMT(A), No.17. National Physical Laboratory Teddington, Middlesex, UK; 1999.

[42] Ogden R, Saccomandi G, Sgura I. Fitting hyperelastic models to experimental data. Computational Mechanics. 2004;34(6):484–502.

[43] Bortoli D, Wrubleski E, Marczak R. Hyperfit – curve fitting software for incompressible hyperelastic material models. 21st Brazilian Congress of Mechanical Engineering (COBEM 2011); 2011 Oct 24–28; Natal (Brazil). p. 1–10.

[44] GB/T 12830. 2008. Rubber, vulcanized or thermoplastic - determination of shear modulus and adhesion to rigid plates - quadruple shear methods.

[45] Michael A, Jose O, Hubert S. Image correlation for shape, motion and deformation measurements - basic concepts, theory and applications. New York: Springer; 2009.

[46] Stanier S, Blaber J, Take WA, et al. Improved image-based deformation measurement for geotechnical applications. Can Geotech J. 2016;53(5):727–739. DOI:10.1139/cgj-2015-0253.

[47] Wu S, Gu L. Introduction to the explicit finite element method for nonlinear transient dynamics. Somerset (USA): John Wiley & Sons, Incorporated; 2012.

[48] Yang Z, Deng X, Li Z. Numerical modeling of dynamic frictional rolling contact with an explicit finite element method. Tribol Int. 2019;129:214–231.

[49] Wang L, Wang P, Wei K, et al. Ground vibration induced by high speed trains on an embankment with pile-board foundation: modelling and validation with in situ tests. Transp Geotech. 2022;34: 100734.

[50] Engineering ToolBox. Friction and friction coefficients; 2004. [online] Available from: https://www.engineeringtoolbox.com/friction-coefficients-d_778.html

[51] Bani-Hani E, Lopez J, Mohanan G. Data on the coefficient of static friction between surfaces coated with different sizes of rubber granules produced from used tires. Data Brief. 2019;22:940–945.

[52] Engineers edge. Available from: https://www.engineersedge.com/coeffients_of_friction.htm

[53] Buehler M, Abraham F, Gao H. Hyperelasticity governs dynamic fracture at a critical length scale. Nature. 2003;426(13):141–146.

[54] Hui C, Jagota A, Bennison S, et al. Crack blunting and the strength of soft elastic solids. Proc Math Phys Eng Sci. 2003;459(2034):1489–1516.

[55] Geng F, Suiker A. An interface damage model for high-cycle fatigue. Eng Fract Mech. 2019;221:106644.

[56] Zou X, Yan S, Matveev M, et al. Experimental and numerical investigation of interface damage in composite L-angle sections under four-point bending. J Compos Mater. 2021;55(2):187–200. DOI:10.1177/0021998320943659.